Effects of Hydrogen Blending Ratio and Fuel Axial Staged Ratio on Methane–Hydrogen Fuel Mixture Combustion Characteristics and NO_x Emission of Double-Swirl Axial Staged Burner

*Xiaochen Yu, Yujie Zhao, Zhen Zhang, Feichi Zhang, and Lin Liu**

Staged combustion is a promising technology that offers a valuable pathway to achieve low NO_x emission in CH_4–H_2 mixed combustion. This study explores the combustion characteristics and NO_x emissions of a double-swirl axial staged burner operating at constant thermal power. The investigation focuses on the synergistic effects of varying fuel axial staged ratios (0.3, 0.5, 0.7) and hydrogen blending ratios (0%–50%) through Fluent numerical simulations. The results indicate that the fuel staged ratio and hydrogen blending ratio are crucial factors influencing the flow field configuration within the combustion chamber, with increased hydrogen blending enhancing fluid kinetic energy and strengthening recirculation zones. It also enhances the combustion temperature and improves the uniformity of temperature. In addition, the hydrogen addition leads to higher temperature and temperature uniformity inside the combustion chamber and the high-temperature zone extends and expands toward the inlet and outlet. Importantly, the appropriate axial staged fuel ratios (0.5) suppress the NO_x generation, with a concentration of less than 150 mg m ^{3} at hydrogen blending ratios ranging from 0% to 30%. This research contributes both a theoretical foundation and a technical pathway for the application of axial staged structures in CH_4–H_2 mixed combustion technology.

1. Introduction

In recent years, various measures have been adopted by many countries to address the issue of greenhouse gas emissions, and controlling global greenhouse gas emissions has become a globally recognized consensus and inevitable trend.[1] Hydrogen is a renewable energy resource and an impeccably clean energy carrier that is capable of achieving zero carbon emissions. The deployment of hydrogen fuel presents a highly promising avenue for the realization of low-carbon combustion objectives. Meanwhile, its characteristics of fast combustion velocity, high combustion temperature, and low ignition energy, it is conducive to optimizing the diffusion combustion of CH_4 fuel, reducing incomplete combustion losses and lowering CO_2 emissions.[2,3] Nevertheless, the blending of hydrogen with alternative fuels can induce heightened temperature conditions, subsequently elevating NO_x concentrations through the thermal NO_x mechanism.[4] Marin et al.[5] discovered that the incorporation of 20% H_2 results in a 7.9% reduction in fuel consumption for gas turbine units, but the combustion chamber temperature slightly increases. Wang et al.[6] studied the response of different modes of nitrogen oxide (NO) generation to hydrogenation in a swirl burner and found that thermal NO increased strongly with the addition of H_2. Currently, the air emission standards published by the Ministry of Ecology and Environment (MEE) of China emphasize that NO_x emissions must be limited to below 150 mg m ^{3}.[7] Therefore, it is meaningful to research the hydrogen blending ratio for combustion and NO_x emission characteristics.

Staged combustion is a widely adopted low-NO_x combustion technique that can be effectively implemented through the decentralized introduction of fuel or air. The two primary forms of implementation are radial staged and axial staged combustion.[8] Liu et al.[9] utilized numerical simulation to optimize the geometric configurations of fuel-staged burners and performed a comprehensive analysis to identify the crucial factors influencing flame dimensions and NO emissions. Xu et al.[10] integrate air-staged combustion with moderate or intense low-oxygen dilution (MILD) combustion to achieve a further reduction in NO emissions by over 80%.Liu et al.[11] investigated staging technology for fuel and air, discovering that increasing fuel stratification can reduce outlet temperatures and significantly decrease NO_x emissions. Elbaz et al.[12]

X. Yu, Y. Zhao, Z. Zhang, L. Liu
School of Mechanical Engineering
Changzhou University
Changzhou 213164, China
E-mail: liulin@cczu.edu.cn

Y. Zhao
Green Process Equipment Key Laboratory of Jiangsu Provincial University
Changzhou University
Changzhou 213164, China

F. Zhang
Institute for Technical Chemistry
Karlsruhe Institute of Technology (KIT)
76128 Karlsruhe, Germany

analyzed the influence of the swirl angle on the combustion characteristics of a double swirl radial staged liquefied petroleum gas (LPG) burner. They found that utilizing a larger internal swirl angle in conjunction with a smaller external swirl angle effectively reduced flame temperature, subsequently leading to a decrease in NO_x emissions. Wang et al.[13] investigated the radially graded combustion of a three-stage fuel and found that adjusting the radial distribution of fuel could reduce the concentrations of NO_x and CO. However, the temperature uniformity of the outlet deteriorated when the fuel was concentrated radially. To sum up, staged combustion technology holds substantial potential for controlling NO_x emissions, and the synergistic effect between radial staged combustion and various combustion technologies has received extensive attention.

In addition, due to the numerous limitations of measurement behavior, many important parameters (such as reaction rates and free radicals) cannot be finely assessed by existing measurement techniques. Numerical simulations are widely used to understand the process of methane–hydrogen combustion in more detail. Lopez-Ruiz et al.[14] studied the fuel jet permeability and combustion byproduct concentration of the Micromax burner by employing the eddy dissipation concept combustion model for simulations. Qin et al.[15] simulated CH_4–H_2 reactive-controlled compression ignition combustion using large eddy simulation (LES) combined with detailed chemical reaction kinetics. Ren et al.[16] employed the LES-pdf model to simulate the combustion state of hydrogen-rich methane in a stratified vortex-tube combustor and analyzed its flame structure and thermodynamic stability. It can be seen that practical and reliable computational fluid dynamics models have been successfully applied to the study of complex CH_4–H_2 burners.

Through the literature review, it can be found that further research is needed to explore the synergistic effects of the axial staged fuel ratio and hydrogen blending ratio on combustion characteristics. This paper uses numerical simulation to study the double-swirl axial staged burner; the simulation domain includes a major part of the nozzle and the combustion chamber. Different computational models are used to consider important physical phenomena such as turbulence, mixing, reactions, component formation, and the interactions between them. The study focuses on analyzing combustion and emission characteristics, including flow field, temperature distribution, CO/CO_2 concentration, and NO_x emission, with the changing fuel axial staged ratio and hydrogen blending ratios.

2. Physical Models and Numerical Simulation

2.1. Burner

This study was conducted on a CH_4–H_2 double-swirl axial staged burner as shown in **Figure 1**. The burner included an air distribution disc and a central fuel distribution tube (central tube) equipped with multiple sets of straight and tapered holes at the end to achieve the radial and axial stage combustion of the fuel. On the one hand, primary fuel entered the combustion zone through the central fuel hole in the central tube, while secondary and tertiary fuels entered through 12 and 18 straight holes, respectively, each 8 mm in diameter. Among them, the central fuel hole spacing is 70 mm, ensuring less interference between fuel jets. On the other hand, the air enters the combustion chamber in a swirl state through a reverse double swirler with an internal swirl angle of 50° and an external swirl angle of 45°. Moreover, 50 mm baffles were provided between the outside of the two-stage swirl and each radial fuel inlet to delay the mixing of fuel and air.

2.2. Numerical Model

In this simulation, the following assumptions are adopted: (1) fluid conforms to the incompressible ideal gas law, (2) stable flow and combustion state, and (3) viscous dissipation is neglected.

(a) Fundamental governing equations

$$\frac{\partial \rho}{\partial t} + \nabla \cdot (\rho \vec{v}) = 0 \tag{1}$$

$$\frac{\partial}{\partial t}(\rho u_i) + \frac{\partial}{\partial x_i}(\rho u_i u_j) = -\frac{\partial p}{\partial x_i} + \frac{\partial \tau_{ij}}{\partial c_j} + \rho g_i + F_i \tag{2}$$

$$\frac{\partial \rho E}{\partial t} + \nabla \cdot (\rho \vec{v} E + \vec{q}) + \nabla \cdot \left(\overline{\overline{T}} \cdot \vec{v} \right) = 0 \tag{3}$$

where ρ is the density, $\vec{v}$ is the velocity, p is pressure, τ_{ij} is the pressure tensor, E is the specific internal energy, $\overline{\overline{T}}$ is the stress tensor, and $\vec{q}$ is the heat flux vector.

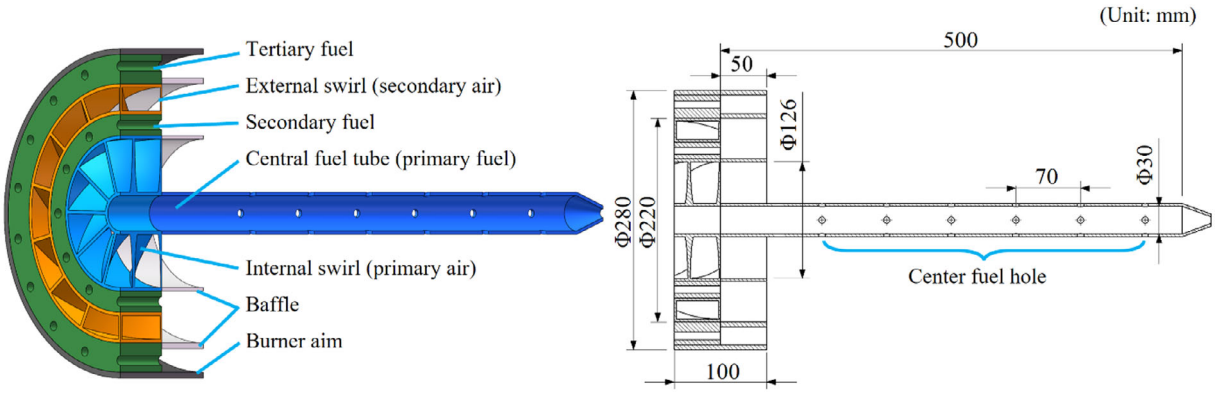

Figure 1. Cross-section view of the burner (left) and dimension marking (right).

(b) Turbulence model

This study selects realizable k–ε as the turbulence model. It has been shown that the use of this model in place of the standard k–ε in swirl and cyclone burners leads to more accurate simulation results.[17] The transport equations for the turbulent kinetic energy (k) and its dissipation rate (ε) are expressed as follows:[18]

$$\rho\frac{dk}{dt}=\frac{\partial}{\partial x_i}\left[\left(\mu+\frac{\mu_t}{\sigma_k}\right)\frac{\partial k}{\partial x_i}\right]+G_k+G_b-\rho\varepsilon-Y_M \tag{4}$$

$$\rho\frac{d\varepsilon}{dt}=\frac{\partial}{\partial x_i}\left[\left(\mu+\frac{\mu_t}{\sigma_\varepsilon}\right)\frac{\partial \varepsilon}{\partial x_i}\right]+\rho C_1 S\varepsilon-\rho C_2\frac{\varepsilon^2}{k+\sqrt{\nu\varepsilon}}+C_{1\varepsilon}\frac{\varepsilon}{k}C_{3\varepsilon}G_b \tag{5}$$

$$\mu_t=\rho C_\mu\frac{k^2}{\varepsilon} \tag{6}$$

where k is the turbulent kinetic energy, ε is the turbulent dissipation rate, μ is the fluid layer laminar viscosity, μ_t is the turbulent viscosity of the fluid, Y_M is a compressible term, $C_{3\varepsilon}$ is the buoyancy term, and G_k and G_b are the turbulent kinetic energies associated with the velocity gradient and buoyancy, respectively.

(c) Radiation equation

The discrete ordinate (DO) radiation model was selected to model and solve for thermal radiation. The transfer equation of the DO radiation model in the $\vec{s}$ direction can be represented in the following.[19]

$$\nabla\cdot(I(\vec{r},\vec{s})\vec{s})+(a+\sigma_s)I(\vec{r},\vec{s})=an^2\frac{BT^4}{\pi}+\frac{\sigma_s}{4\pi}\int_0^{4\pi}I(\vec{r},\vec{s}')\Phi(\vec{s},\vec{s}')d\Omega' \tag{7}$$

where I is the radiation intensity, $\vec{r}$ is the position vector, $\vec{s}$ is the direction vector, $\vec{s}'$ is the scattering direction vector, σ_s is the scattering coefficient, Φ is the phase function, Ω' is the solid angle, a is the absorption coefficient, and B is the Stephen–Boltzmann constant.

(d) Combustion model

A two-step reaction of CH_4 and a one-step reaction of H_2 were selected to realize the combustion process required in this study.[20] The reaction equation and relevant parameters are summarized in **Table 1**.[21,22]

The finite rate/eddy dissipation model (FR/EDM) was selected as the combustion model, and the corresponding reaction rate equations involved are presented in Equation (8), Equation (9), and Equation (10)[23]

$$k_{f,r}=A_r T^{\beta}\exp\left(-\frac{E_a}{RT}\right) \tag{8}$$

$$R_{i.r}=\nu'_{i,r}M_{w,i}A\rho\frac{\varepsilon}{k}\min_R\left(\frac{Y_R}{\nu'_{R,r}M_{w,R}}\right) \tag{9}$$

$$R_{i.r}=\nu'_{i,r}M_{w,i}AB\rho\frac{\varepsilon}{k}\frac{\sum_P Y_p}{\sum_j^N \nu''_{j,r}M_{w,j}} \tag{10}$$

where A_r is the pre-exponential factor, β_r is the temperature exponent, T is the temperature, E_a is the activation energy, $k_{f,r}$ is the reaction rate coefficient, $\nu'_{i,r}$ is the stoichiometric coefficient (reactant i in reaction r), $M_{w,i}$ is the molecular mass of species i, Y_R is the mass production of species R, Y_p is the mass production of species P, $\nu''_{i,r}$ is the stoichiometric coefficient of product j in reaction r, R is the universal gas constant, and A, B are the empirical constants ($A=4.0$, $B=0.5$).[24]

(e) NO model (thermal type and NNH route)

Air is primarily composed of O_2 and N_2. Although N_2 is considered a neutral and inert gas in chemical reactions at room temperature, it can be activated into highly reactive molecules at elevated temperatures. When N_2 and O_2 interact at high temperatures, various NO_x harmful to human health and the environment are produced, contributing to air pollution.[25] The Zeldovich mechanism is commonly employed to describe the generation of thermal NO_x[26]

$$N_2+O\overset{k_{f,1}}{\underset{k_{r,1}}{\leftrightarrow}}NO+N \tag{11}$$

$$N+O_2\overset{k_{f,2}}{\underset{k_{r,2}}{\leftrightarrow}}NO+O \tag{12}$$

$$N+OH\overset{k_{f,3}}{\underset{k_{r,3}}{\leftrightarrow}}NO+H \tag{13}$$

The rate equation for the reaction can be expressed by Equation (14), and the reaction rate constants for each reaction are listed in **Table 2**

$$\frac{d[NO]}{dt}=2k_{f,1}[O][N_2]\frac{\left(1-\frac{k_{r,1}k_{r,2}[NO]^2}{k_{f,1}[N_2]k_{f,2}[NO]^2}\right)}{\left(1+\frac{k_{f,1}[NO]}{k_{f,2}[O_2]+k_{f,3}[OH]}\right)} \tag{14}$$

The NNH route is also an important NO generation mode in the CH_4–H_2 mixed combustion process.[27] Its reaction equation can be expressed by Equation (15) and Equation (16)[28]

$$N_2+H\leftrightarrow NNH \tag{15}$$

Table 1. Reaction equation and parameters.

Reaction	Pre-exponential factor A_r [s^{-1}]	Activation energy E_a [J $kmol^{-1}$]
$CH_4+1.5O_2\rightarrow CO+2H_2O$	5.012×10^{11}	2×10^8
$CO+0.5O_2\rightarrow CO_2$	2.239×10^{12}	1.7×10^8
$H_2+0.5O_2\rightarrow H_2O$	9.87×10^8	3.1×10^7

Table 2. Reaction rate constant of thermal NO formation.

Forward reaction [$m^3\ mol^{-1}\ s^{-1}$]		Backward reaction [$m^3\ mol^{-1}\ s^{-1}$]	
$k_{f,1}$	$1.8\times10^8\exp(-38370\,T^{-1})$	$k_{r,1}$	$3.8\times10^7\exp(-425\,T^{-1})$
$k_{f,2}$	$1.8\times10^4T\exp(-4580\,T^{-1})$	$k_{r,2}$	$3.81\times10^3T\exp(-20820\,T^{-1})$
$k_{f,3}$	$7.1\times10^7\exp(-450\,T^{-1})$	$k_{r,3}$	$1.7\times10^8\exp(-24560\,T^{-1})$

$$NNH + O \leftrightarrow NH + NO \quad (16)$$

The reaction rate of the NNH route obtained based on the above reaction is as follows:[29]

$$\frac{d[NO]}{dt} = 2k_2 K_{p1}[N_2][O]X_H \quad (17)$$

$$k_2 K_{p1} = 2.3 \times 10^{15} \exp\left(\frac{-2760}{T}\right) \quad (18)$$

where K_{p1} is the equilibrium constant of Equation (15) expressed in partial pressures, and X_H is the mole fraction of H atoms.

2.3. Boundary Conditions and Solution Settings

In this study, mass flow boundary conditions were applied to both the air and fuel inlets, and pressure outlet boundary conditions were implemented for the outlet. The combustion chamber wall was assigned a convective thermal boundary condition, and the effects of flow and heat transfer within the wall boundary layer were calculated using the enhanced wall function method. The convective heat transfer coefficient was set to 50 W m^{-2} K^{-1}, while the free stream temperature was maintained at 358 K. All simulations were performed with a fixed O_2 fraction of 21% in air, a constant heat load of 500 kW, and an excess air coefficient of 1.1.

This research conducted computing tasks on a small tower server equipped with an AMD EPYC 9654 processor, which features a total of 96 physical cores and 256 GB of memory. The three-dimensional diffusion combustion of CH_4–H_2 is simulated using the finite volume method, employing Ansys Fluent 2022R1 software. The weighted sum of gray gases model was selected to calculate the gas absorption coefficient, accounting for the non-gray radiative properties of the gas.[30] The SIMPLE algorithm was utilized to solve the discrete equations for pressure–velocity coupling, while the PRESTO! method was employed for pressure discretization. The first-order upwind scheme was applied to the radiation equation, whereas second-order schemes were implemented for the remaining equations to achieve more precise solutions.[31] The convergence criterion was established to ensure the accuracy of the iterative computational process.[32] Specifically, the residual of the continuity equation was constrained to be less than 10^{-4}, while the residuals of the energy and radiation equations were required to be less than 10^{-6}. Additionally, the residuals of the other equations were constrained to be less than 10^{-5}. The more comprehensive simulation scheme for the computational model is shown in **Table 3**. The control equations and applicability are more systematically described and demonstrated in other published literature.[33,34]

Table 3. Model settings.

Items	Value	Remarks
Time	Steady	–
Turbulence	Realizable k-ε	Enhanced wall function
Reaction	–	–
Volume reaction	FR/Eddy dissipation	–
CH_4 reaction (2 steps)	$CH_4 + 1.5O_2 \rightarrow CO + 2H_2O$	–
	$CO + 0.5O_2 \rightarrow CO_2$	–
H_2 reaction (1 step)	$H_2 + 0.5O_2 \rightarrow H_2O$	–
NO_x	Thermal NO and NNH routes	–
Radiation	DOs	–
Physical property	–	–
Density	Incompressible ideal gas	–
Specific heat	Mixing law	–
Thermal conductivity	Mass-weighted mixing law	–
Absorption coefficient	WSGGM domain-based	–
Solution method	–	–
Solver	SIMPLE	Pressure-based
Pressure	PRESTO!	–
Turbulence	Second-order upwind	–
Species	Second-order upwind	–
Radiation	First-order upwind	–

2.4. Grid and Independence Verification

Given the significant impact of the internal flow generated by the double swirl of the burner on the downstream combustion process, the calculation domain covering the main part of the nozzle is specially established. **Figure 2** displays the 3D poly-hexcore mesh of the entire combustion zone domain, generated using Ansys meshing software. The cylindrical-shaped combustion chamber with rounded corners has the dimensions of length × diameter = 2500 × 600 mm, rounded radius = 150 mm. The terminal face of the air distribution disc is taken as the $x = 0$ plane, and the main flow direction of the gas is taken as the positive direction of the x-axis. A boundary layer was established on the wall to more accurately reflect the flow characteristics of the fluid. Due to the complex chemical reactions concentrated in the area near the burner, the grid of the area related to the inlet and the central fuel hole is locally refined.

To evaluate the influence of the grid number on the results, the same partitioning method was adopted, gradually increasing the grid number to verify the independence of the grid while ensuring that the minimum orthogonal quality remained above 0.35. Furthermore, the maximum aspect ratio is 39.65. Four different mesh configurations consisting of 1,631,583, 2,931,371, 4,974,378, and 6,839,549 cells were selected for comparison. The maximum combustion temperature and the weighted average of NO_x concentration at the outlet with the hydrogen mixing ratio of 30% and the primary fuel ratio of 0.5 were selected as the grid independence check parameters, with the results presented in **Figure 3**. It can be observed that the maximum temperature and NO_x concentration change less than 1% when the number of grids is more than 2,931,371. Consequently, taking into account the need to maintain a balance between accuracy in computations and overall efficiency, a grid model comprising 2,931,371 grids was utilized in the follow-up research.

Furthermore, taking the maximum outlet temperature and NO_x concentration as the evaluation criteria, the grid convergence index (GCI) was calculated. The calculation method of

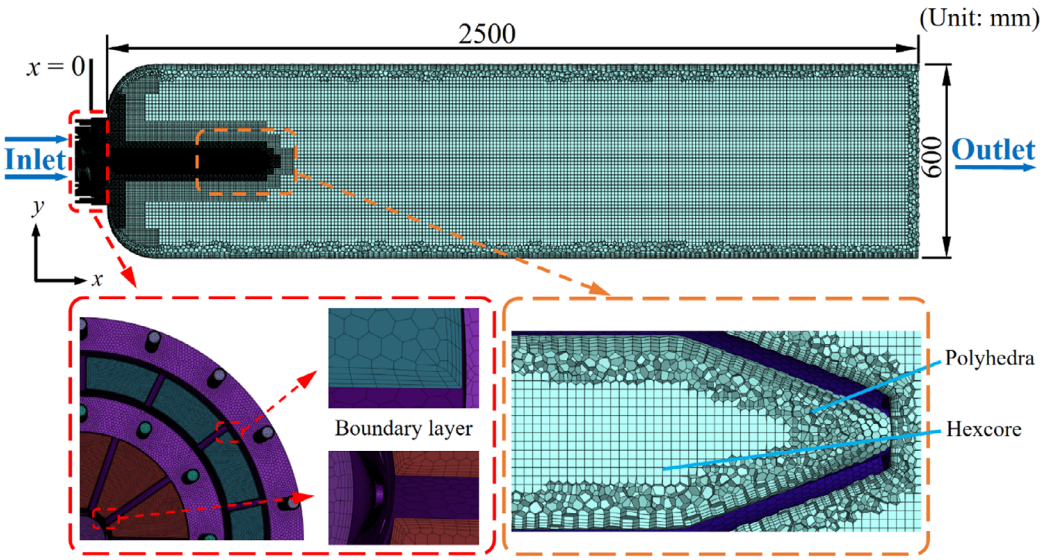

Figure 2. 3D combustion chamber model and poly-hexcore grid.

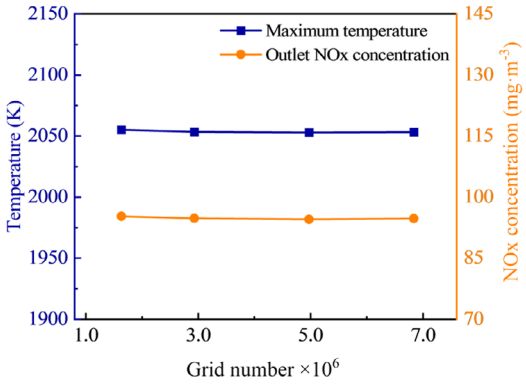

Figure 3. Grid independence verification.

Table 4. Grid GCI results.

Evaluation index	Grid number	Number of grid nodes	Grid encryption ratio	Convergence error	GCI/%
Maximum temperature	1631583	3769875	1.172	–0.00078	0.27
	2931371	6075884	1.178	–0.00028	0.09
	4974378	9923955	1.115	0.00015	0.08
	6839549	13769194	–	–	–
Outlet NO_x concentration	1631583	3769875	1.172	–0.00485	1.65
	2931371	6075884	1.178	–0.00275	0.90
	4974378	9923955	1.115	0.00180	0.94
	6839549	13769194	–	–	–

GCI has been described in detail in the literature.[35,36] The results are shown in **Table 4** and can be found that when the number of grid cells is greater than 2,931,371, the GCI values under both indicators are less than 3%–5%, that is, the continuous increase of grids has no impact on the results. Consequently, it is feasible to select the grid configuration of 2,931,371 for subsequent simulations.

2.5. Model Validation

2.5.1. Detailed Mechanism Verification

This study adopts a simplified global mechanism for calculations, and the accuracy of its combustion temperature needs to first be verified against the widely recognized detailed mechanism GRI 3.0.[37] **Figure 4** illustrates the comparison of temperature distributions between the global and detailed mechanisms along the x-direction cross section. The results depicted in the figure demonstrate a similarity in the temperature distributions of both mechanisms, with the maximum error remaining below 5%. Therefore, it can be considered that the global mechanism

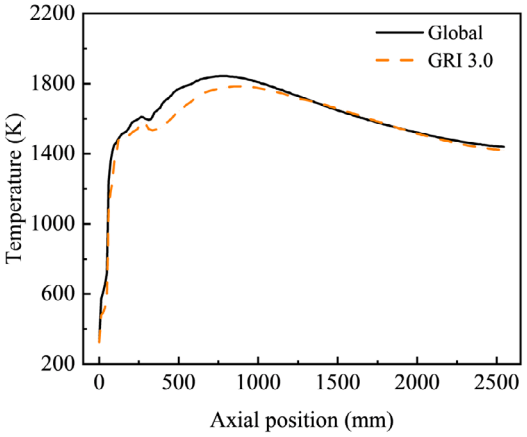

Figure 4. Mechanism verification of temperature distribution.

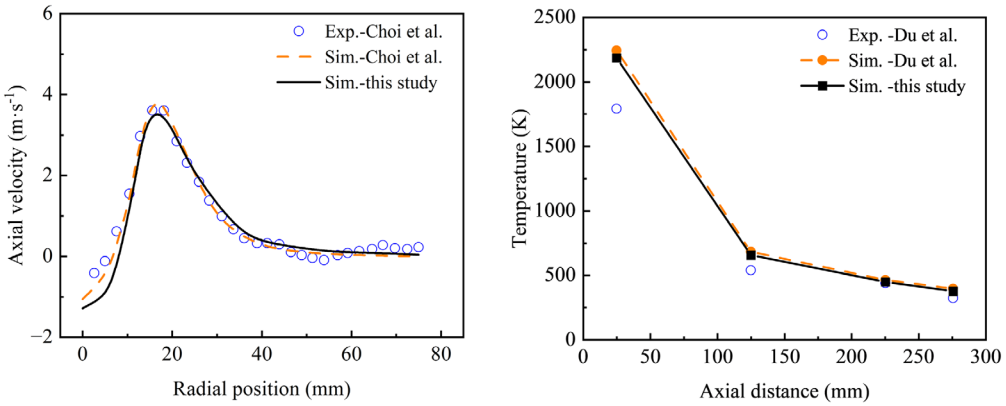

Figure 5. Model validation. Axial velocity (left) and temperature (right).

adopted in this study can basically reflect the combustion characteristics of the mixed combustion of CH_4–H_2.

2.5.2. Experimental Verification

It is permissible to independently compare the experimental data from different CH_4–H_2 swirl burners to validate the mathematical model's feasibility.[38] On the one hand, the validation of the flow component within the mathematical model employed in this research was conducted using the experimental data of axial velocity from the double-swirl burner during pure methane combustion, as reported by Choi et al.[22] as shown in **Figure 5** (left). The figure shows that the maximum deviation between the simulation results and experimental values is less than 10%, indicating that the current mathematical model can accurately reflect the flow process. On the other hand, for thermodynamic validity, the relevant parameters and experimental data from the CH_4–H_2 swirling combustor reported by Du et al.[39] were used for verification. The comparison of the temperature distribution at the axial position, with a hydrogen content of 20%, is illustrated in Figure 5 (right) by contrasting the calculated values with the experimental ones. Due to the ideal gas assumption in the numerical simulation, the incomplete mixing of fuel during experimental measurements, and the interference of measurement equipment with the flow field, some inaccuracy is expected.[40] However, the overall temperature trend remains consistent, demonstrating that the numerical model effectively captures the thermodynamic characteristics. Therefore, it can be concluded that the numerical code correctly characterizes the combustion process.

3. Results and Discussion

Since CH_4 and H_2 have different physicochemical properties and combustion characteristics, the combustion performance of a double-swirl axial staged burner, under constant heat load and equivalent ratio, largely depends on the hydrogen blending ratio (X_{H_2}). This ratio significantly influences the overall characteristics of the burner, more so than the minor changes in inlet velocity caused by the partial replacement of CH_4 with H_2.[41] The hydrogen blending ratio is represented by Equation (19).[42]

Furthermore, as a crucial parameter for axially staged combustors, the fuel axial staged ratio (X_{fuel_1}) also significantly impacts combustion, as expressed by Equation (20)

$$X_{H_2} = \frac{V_{H_2}}{V_{H_2} + V_{CH_4}} \tag{19}$$

$$X_{fuel\_1} = \frac{V_{fuel\_1}}{V_{fuel}} \tag{20}$$

where V_{CH_4} and V_{H_2} are, respectively, the volume fractions of CH_4 and H_2 in the fuel, V_{fuel_1} is the main fuel volume flow, V_{fuel} is the total fuel volume flow.

To investigate the effects of the synergistic interaction between X_{fuel_1} and X_{H_2}, the combustion emission characteristics at the CH_4–H_2 staged burner, six typical X_{H_2} of 0%, 10%, 20%, 30%, 40%, and 50% were set up at X_{fuel_1} of 0.3, 0.5, and 0.7 in this paper. **Table 5** shows the setting parameters for various hydrogen blending ratios.

Table 5. Parameter settings for different hydrogen blending ratios.

Project	Unit	Hydrogen blending ratios					
		0	10%	20%	30%	40%	50%
Fuel inlet mass flow rate	(kg h^{-1})	36.00	35.32	34.53	33.60	32.49	31.15
Air inlet mass flow rate	(kg h^{-1})	685.24	681.51	677.17	672.07	665.97	658.56
Fuel axial staged ratio	/	0.3/0.5/0.7					
Secondary and tertiary fuel volume ratio	/	2:3					
Air staged volume ratio	/	1:1					
Thermal load	kW	500					
Excess air coefficient	/	1.1					
Outlet pressure (relative)	Pa	–200					

3.1. Flow Field Distribution

Fuel axial staged ratio and hydrogen blending ratio are both important factors affecting flow field morphology. **Figure 6** presents the distribution of the axial velocity (top) and velocity streamlines (bottom) in the middle plane of the combustion chamber ($X_{H_2} = 0$, 30%, 50%). It can be observed that a distinct V-shaped region induced by swirling flow, along with two counter-rotating circulation zones situated both within and outside this region, is clearly discernible in the flow field. It is noteworthy that as the hydrogen blending ratio increases from 0% to 50%, the axial high-speed region significantly expands. This indicates that hydrogen-blended combustion effectively enhances the kinetic energy of the fluid, and the high combustion velocity of hydrogen effectively promotes the high-speed motion of the fluid. Specifically, increasing the hydrogen blending ratio enhances the local combustion rate, which accelerates the rotational speed at the front part of the V-shaped zone and expands the inner recirculation area. Further analysis indicates that as the proportion of hydrogen increases, the combustion reaction occurs more rapidly, releasing energy more quickly within a shorter time frame and limited space. This rapid combustion amplifies local pressure fluctuations and turbulence intensity, promoting the swift expansion of combustion flue gas. Consequently, this enhances momentum exchange within the vortex and strengthens the development of the recirculation zone.[43]

By comparison, the fuel axial staged ratio significantly affects the V-shaped zone. The rotating airflow directly impacts the front wall of the burner and gradually moves toward the rear along the wall, with the tangential circulation gradually weakening. Direct injection of central fuel into the V-shaped region induces substantial changes in the inner recirculation zone. Specifically, the primary fuel flow's lower kinetic energy creates a difference in velocity with the V-region's front to maintain a large inner recirculation zone at $X_{fuel\_1} = 0.3$. As the fuel axial stage ratio increases, the flow rate of the V-shaped main swirl decreases and a greater proportion of fuel being directly injected from the central pipe into the center area of the swirl. This change results in a compression of the inner recirculation zone. Additionally, both the secondary and tertiary fuels, along with the double-swirl air, enter the combustion chamber through the distribution disc, forming a swirling mixture that directly impinges on the combustion chamber wall. This creates partially detached turbulent structures at the edges of the swirl, and the difference in swirl entrainment capability caused by different flow velocities of the main swirl also result in changes in the inner recirculation zone.

Figure 7 plots the axial velocity in the cross-section position of the combustion chamber, illustrating that when the secondary and tertiary fuels and swirling air enter the combustion chamber, the axial velocity rapidly decreases. It then experiences a gradual ascent and undergoes a mild attenuation in the area rear of the central tube, ultimately attaining a near-stable flow condition as it reaches the outlet. This trend is consistent with the findings of Xiao et al.[41] Ulteriorly, with the increase of hydrogen blending ratio, an increase in the minimum axial velocity was observed in the region of $x =$ 110–460 mm (central fuel hole influence zone). Specifically, the axial velocity of $x =$ 110 mm cross section (left-center fuel port) is taken as a reference. For $X_{fuel\_1} =$ 0.3, when the X_{H_2} increases from 0% to 50%, the corresponding axial velocities are 0.98 and 2.24 m s^{-1}, respectively, with an increase of 1.26 m s^{-1}. Similarly, for X_{fuel_1} of 0.5 and 0.7, the axial velocity, respectively, increases 0.97 and 0.75 m s^{-1}. This can be attributed to higher fuel flow rates and a more intense reaction of H_2. It is worth mentioning that the increase in fuel axial staged ratio also compresses the range of axial velocity variation but shifts the position of velocity attenuation backward.

3.2. Combustion Temperature Distribution

In this study, the temperature distribution within the middle plane of the combustion chamber is analyzed, as illustrated in **Figure 8**. In a swirling stable flame, CH_4–H_2 fuel in the central tube is injected axially into the combustion zone, forming a local low-temperature zone in the inner recirculation zone. The occurrence of a highly swirling flow creates a V-shaped temperature distribution within the combustion chamber, which aligns with

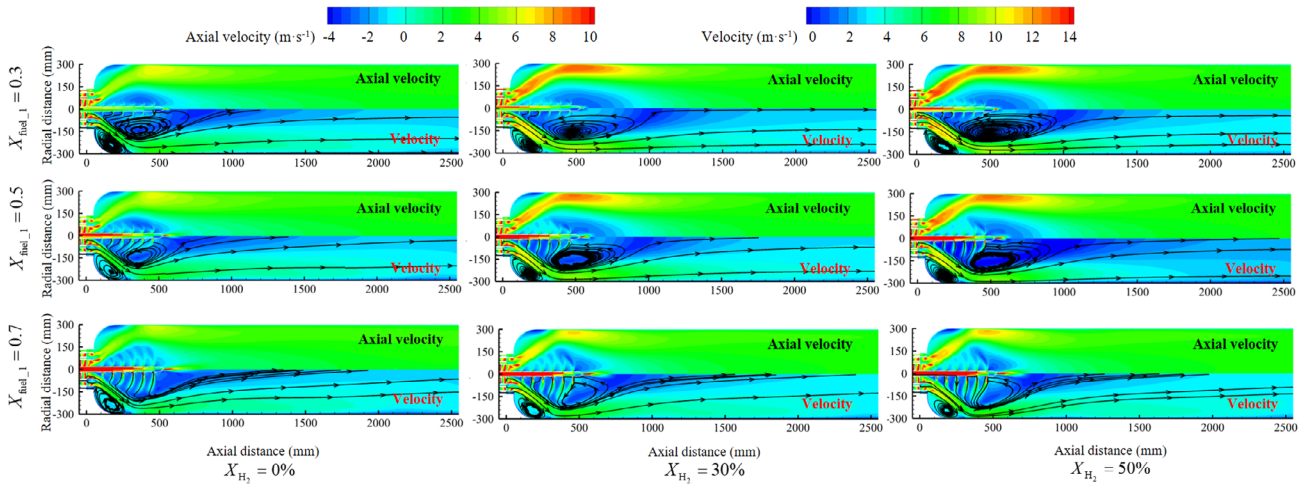

Figure 6. Axial velocity (top) and velocity streamline (bottom) distribution ($X_{H_2} =$ 0, 30%, 50%).

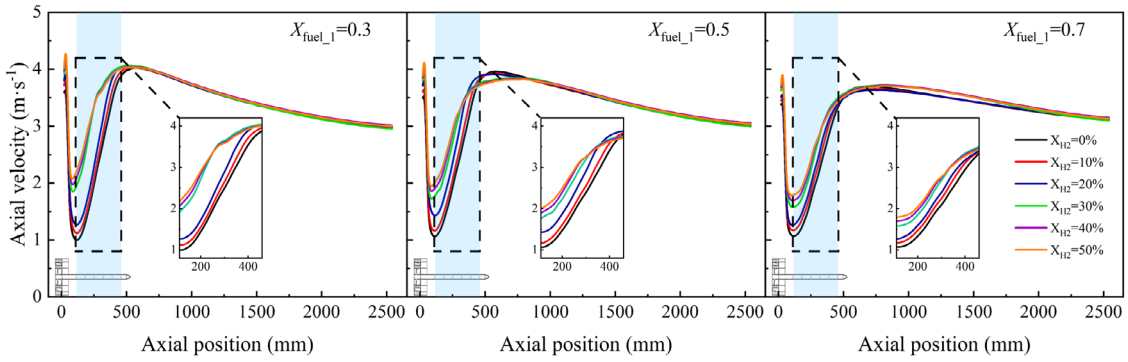

Figure 7. Axial velocity in cross-section position of the combustion chamber.

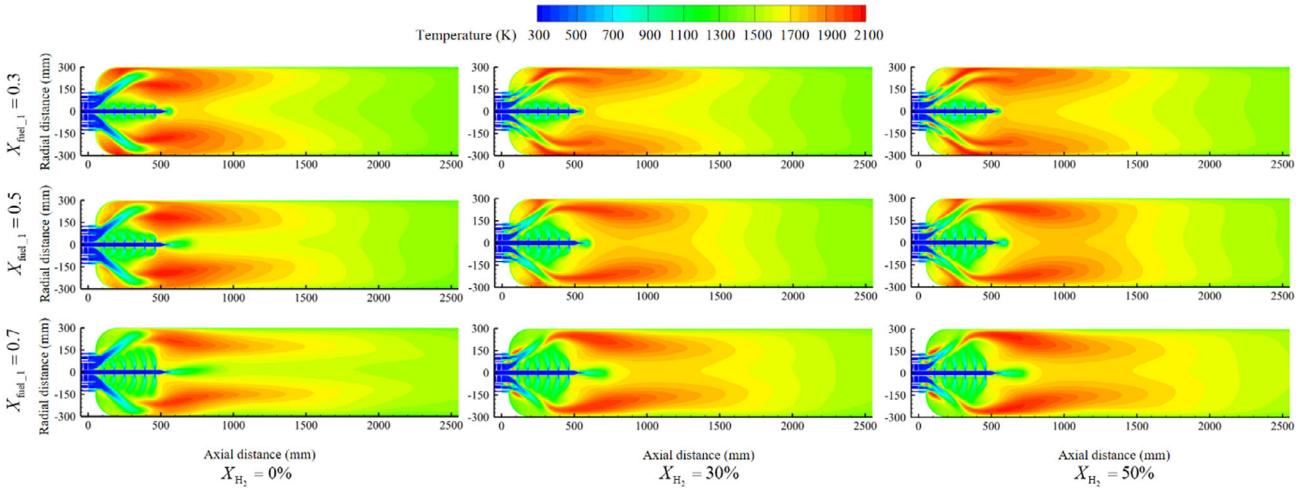

Figure 8. Temperature distribution (X_{H_2} = 0, 30%, 50%).

the flow field distribution illustrated in Figure 6. As the hydrogen blending ratio increases from 0% to 50%, the combustion rate of the mixed fuel accelerates, evidenced by the high-temperature region progressively shifting closer to the burner distribution plate. This phenomenon occurs because H_2 combusts more rapidly and releases more heat at the front end of the combustion chamber compared to methane. Notably, increasing the proportion of X_{fuel_1} or X_{H_2} extends the flame length. The constant energy input leads to a decreased fuel density and increased flow rate, combined with larger axial fuel staging that hinders adequate fuel–air mixing, thereby enlarging the reaction zone.

Figure 9 (top) demonstrates the average temperature on the cross section of the combustion chamber. Clearly, the overall temperature increases as the hydrogen blending ratio increases, especially in the back part of the central tube, which corresponds with the results shown in Figure 8. Meanwhile, the introduction of H_2 significantly reduces the activation energy of the mixed fuel, moves the position of the fuel oxidation reaction forward, and there is also a phenomenon of increased combustion temperature in the influence zone of the central tube.[44] In addition, increasing X_{fuel_1} leads to fuel buildup in the internal circulation zone, resulting in a decrease in temperature in the central fuel hole influence zone. The temperature uniformity metric used to evaluate uniformity is given in Figure 9 (bottom), where a value of 1 indicates the highest uniformity. Increasing X_{H_2} enhances temperature uniformity because the higher diffusivity of H_2 ensures a more uniform mixing and heat release of the fuel and air. And increasing the proportion of the main fuel can also enhance it through the effect of fuel redistribution. However, due to the long free diffusion zone at the combustion chamber, this effect is negligible for the outlet.

Figure 10 demonstrates the influence of the hydrogen blending ratio on the high-temperature regions (above 1600 K) proportion and outlet temperature of the combustion chamber for three different fuel axial staged ratios, and it is found that the high-temperature zone and outlet temperature expand significantly with the increase of hydrogen mixing ratio. In conjunction with the simulation data, when $X_{fuel\_1} = 0.5$, the high-temperature range expands from 54.9% to 61.5% and the outlet temperature increases from 1435.44 to 1476.67 K as the X_{H_2} increases from 0 to 50%. This phenomenon can be attributed to the fact that the adiabatic flame temperature of hydrogen (2400 K) is higher than that of methane (2200 K), which results in a higher local temperature and an expanded range of high-temperature zones. In addition, since the heat transfer coefficient of the wall is

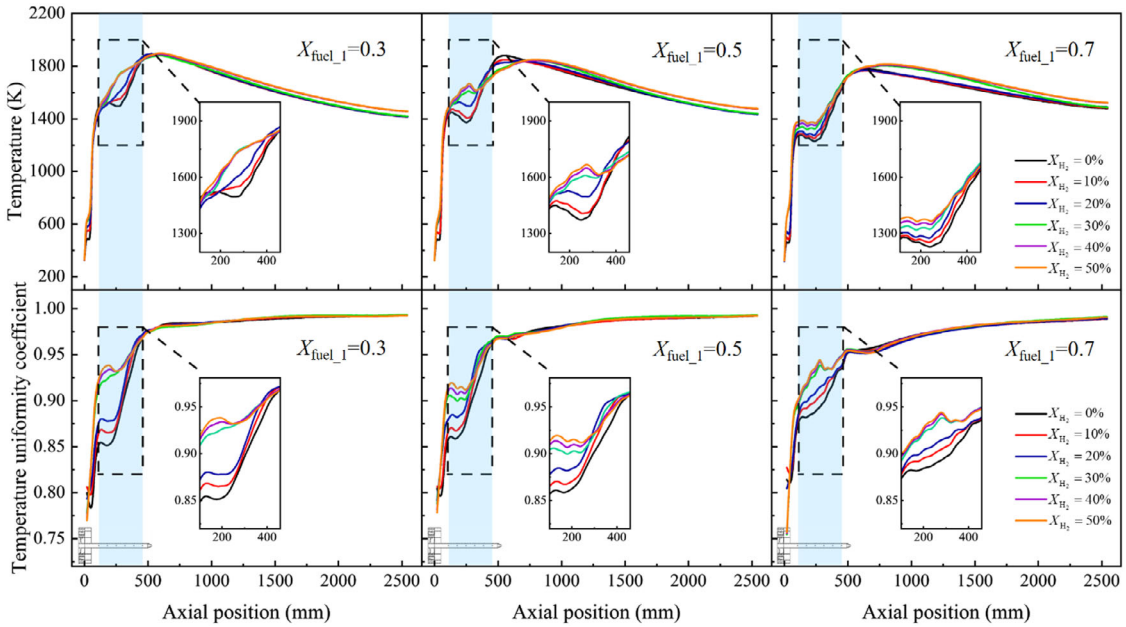

Figure 9. Temperature (top) and temperature uniformity coefficient (bottom) in the cross-section position of the combustion chamber.

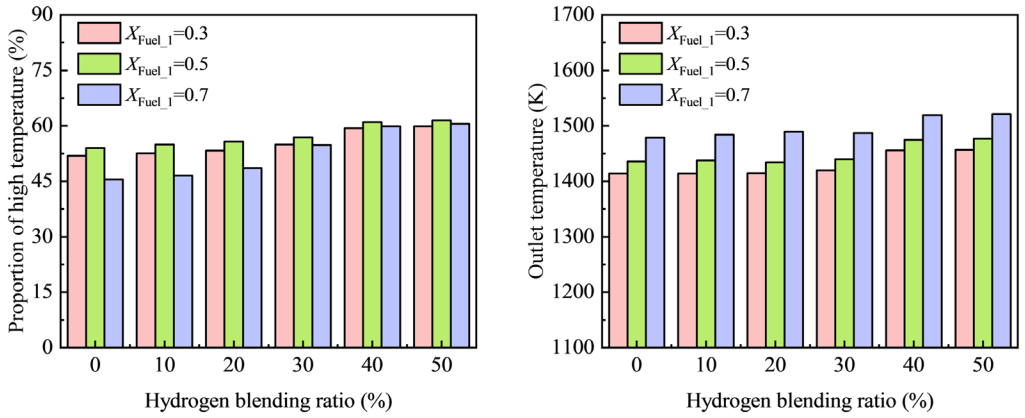

Figure 10. The proportion of the high-temperature zone (left) and outlet temperature (right).

assumed to be constant, the elevated combustion temperature in the combustion zone results in an increase in the outlet temperature. At a higher fuel axial staged ratio ($X_{fuel\_1} = 0.7$), a higher proportion of high-temperature zones and outlet temperatures are observed due to the reduced mixing effect of fuel and air, which causes the reaction to be unable to proceed as quickly and allows the sustained release of energy over a larger axial length.

3.3. CO and CO_2 Emissions

The oxidation combustion reaction of alkane fuels is often incomplete; some are only oxidized to CO and not converted to CO_2.[45] Mechanistically, during the combustion of gaseous alkane fuels, hydrocarbon molecules do not decompose due to a localized lack of O_2, which leads to the formation of CO. Therefore, analyzing the concentration of CO can effectively serve as an indicator of methane combustion efficiency, thereby reflecting the utilization rate of the mixed fuel.

Figure 11 illustrates the distribution of CO and CO_2 concentrations. At a fuel axial staged ratio of 0.3, the outlet CO concentration was measured at 3.44×10^{7} when $X_{H_2} = 0\%$, decreasing to 9.39×10^{9} at $X_{H_2} = 50\%$, representing a reduction of 97%. For the fuel axial staged ratio of 0.5, the CO concentration decreased by 95% from 2.43×10^{5} and 1.17×10^{6} when $X_{H_2} = 0\%$ to 50%, respectively. Similarly, when $X_{fuel\_1} = 0.7$, the CO concentration decreased from 5.56×10^{4} to 1.19×10^{4}, a decrease of 78%. Combined with Figure 11 (left), it is further evident that a higher graded fuel ratio leads to the generation of a denser CO concentration during the initial phase of combustion, attributable to an elevated equivalent ratio within the inner zone. Despite recirculation, the inadequate mixing of fuel and air that hinders the complete

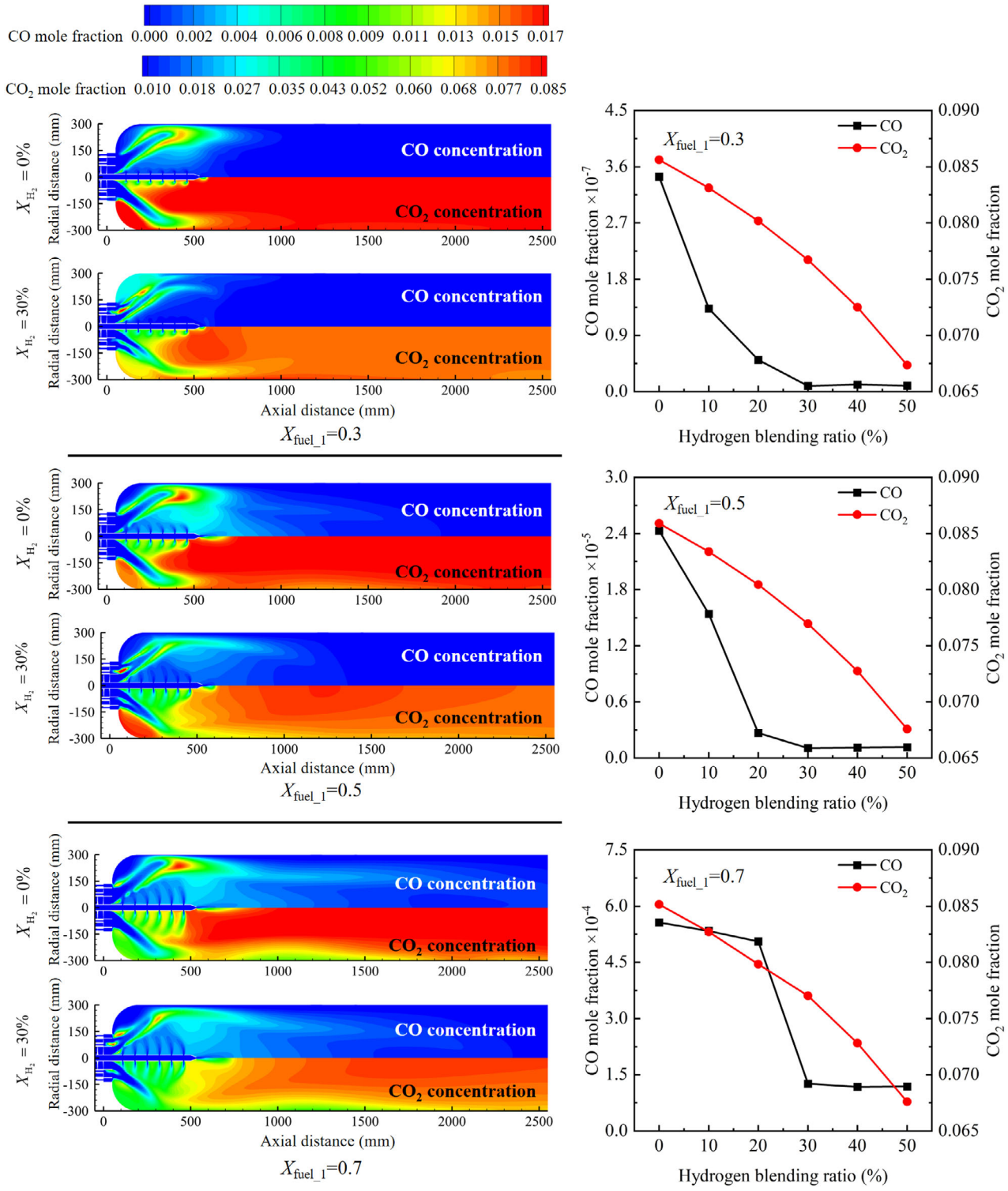

Figure 11. CO and CO_2 distribution at X_{H_2} = 0, 30% (left) and outlet concentration (right).

oxidation of CO in the combustion chamber, the introduction of H_2, particularly when its content surpasses 30%, markedly decreases the CO concentration, indicating that H_2 has a notable effect on alleviating incomplete combustion under fuel-rich conditions. However, it does not eliminate the effects because of the limited diffusion capacity and delayed mixing locations.

In addition, in comparison to pure methane fuel, the hydrogenation process significantly reduces the outlet CO_2

concentration at each axial stage ratio of the fuel, with the reduction rate progressively accelerating. Specifically, as the hydrogen content increases to 50%, the CO_2 concentration decreases by 2.5%, 6.4%, 10.4%, 15.3%, and 21.3% (compared to a hydrogen content of 0%). This reduction can be attributed to the increased hydrogen blending ratio, which progressively decreases the carbon content in the mixed fuel.

3.4. NO_x Emissions

Figure 12 illustrates the distribution of the NO generation rate (top) and NO concentration (bottom) during the combustion process. It is evident that NO is primarily produced at the front of the combustion chamber and accumulates progressively. This phenomenon occurs because NO in the NNH route is rapidly produced at the point where fuel and air begin to mix, with the higher temperature in this area also leading to substantial thermal NO generation.[46] Moreover, a comparison with Figure 8 shows that the distribution of the NO generation rate aligns closely with the distribution in the high-temperature region, consistent with the findings reported by Cheng et al.[47] Specifically, NO generation is primarily concentrated at the leading edge of the V-region (the fuel–air contact surface) and increases with the hydrogen blending ratio, particularly at X_{fuel_1} values of 0.3 and 0.7. Notably, at $X_{fuel\_1} = 0.5$, there is a marked inhibitory effect on NO generation. This is because local high temperatures promote the formation of NO, but the temperature is reduced through the implementation of axial fuel staging. Further analysis indicates that this structural modification extends the mixing distance between fuel and air, thereby diminishing combustion intensity.

Figure 13 shows the distribution of maximum temperature (left) and outlet NO_x concentration (right). In terms of the generation mode of NO_x, since the reaction rate of thermal NO_x production is an exponential function of temperature, leading to a strong correlation between thermal NO_x concentration and maximum temperature.[48] As the proportion of H_2 entering the combustion chamber increases, the elevated combustion flame temperature facilitates NO formation, resulting in a higher total outlet NO_x concentration. This is attributed to the significantly higher lower heating value of H_2 compared to methane fuel[34] and the increased hydrogen blending ratios of the combustion temperature of the CH_4–H_2 mixture.[49] Regarding the NNH generation pathway of NO_x, the combustion of hydrogen releases

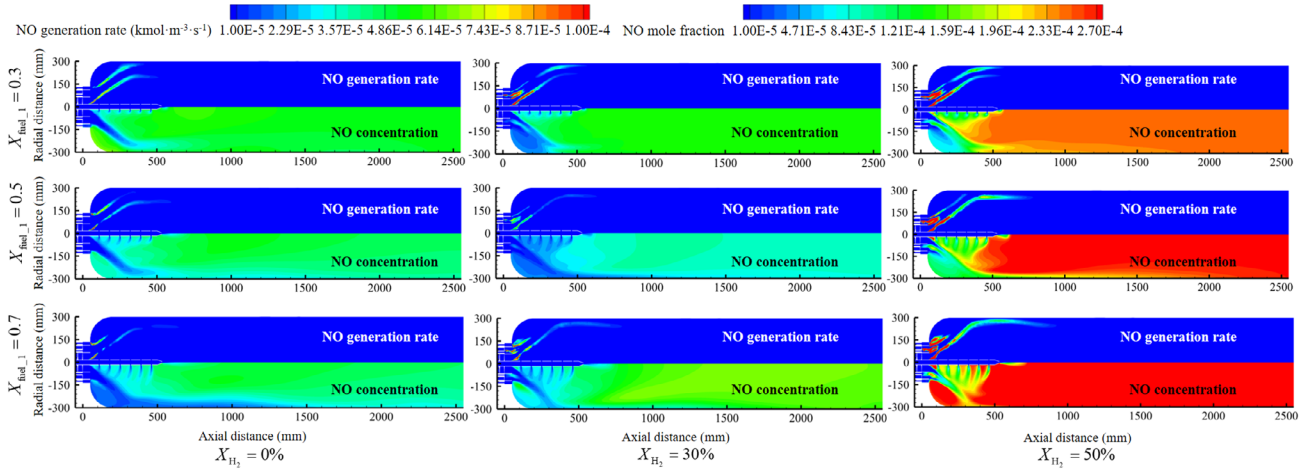

Figure 12. Comparison of the NO generation rate (top) and NO concentration (bottom) distribution (X_{H_2} = 0, 30%, 50%).

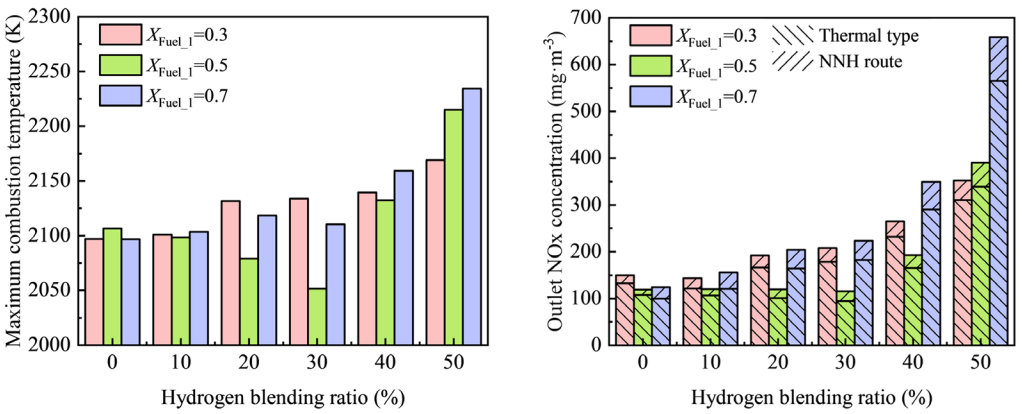

Figure 13. Comparison of the maximum combustion temperature (left) and outlet NO_x concentration (right).

a significant number of H radicals, which directly promotes the formation of NNH-type NO.[50] Therefore, as the hydrogen blending ratio increases, the concentration of NO generated via the NNH route consistently increases within the total NO_x concentration. At relatively low hydrogen blending ratios (0%–20%), an increase in hydrogen content results in a higher proportion of NNH in the total NO_x concentration. However, when the hydrogen blending ratio further increases (30%–50%), the production of NO_x due to elevated temperatures increases substantially, leading to a decrease in its relative contribution rate. Overall, compared to thermal NO, the significance of the NNH route is relatively lower. This phenomenon can be attributed to the fact that the air selected in the combustion chamber has an oxygen volume fraction of 21%, and both H_2 and CH_4 are effectively consumed through reactions with O_2, which significantly increases the temperature in the combustion chamber. As a result, the thermal NO route predominates in the formation of NO.[51,52] In addition, in terms of axial fuel staging, the axial supply of fuel effectively alleviates the problem that the addition of hydrogen to fuel often advances the location of the fuel oxidation reaction and increases the local heat release associated with this reaction.

Consequently, this structure reduces the peak combustion temperature to some extent, thereby preventing the large-scale formation of NO_x. For instance, at a hydrogen blending ratio of 30%, the NO_x concentration of $X_{fuel\_1} = 0.5$ reaches 115.78 mg m^{-3}, which is 92.38 mg m^{-3} lower than that of $X_{fuel\_1} = 0.3$ and 34.22 mg m^{-3} lower than that of the emission standard (150 mg m^{-3}). Compared to the NO_x concentrations when X_{fuel_1} is 0.3 and 0.7, this represents reductions of 44% and 48%, respectively. This can be attributed to the effective extension of the high-concentration distribution of fuel to the front and middle of the combustion area by broadening the range of the fuel–air mixture. This structure prevents the rapid mixing of fuel with the rotating air at the front of the V-shaped area, thereby avoiding excessive local temperatures. Meanwhile, due to the weakened high-concentration enrichment behavior of the mixed hydrogen fuel in the front part of the combustion chamber, the local high-enrichment environment of H radicals is reduced, which also inhibit the generation of NO under the NNH route to a certain extent. However, when the fuel axial staged ratio is as high as 0.7, a large amount of fuel accumulates in the V-shaped area, and the fuel axial staging capability is weak, resulting in no significant inhibitory effect on NO_x generation.

4. Conclusion

In this study, the combined effects of hydrogen blending ratio and fuel axial staged ratio on combustion and NO_x emission characteristics of a CH_4–H_2 double-swirl axial staged burner were investigated. The results from these studies are presented below. 1) increasing the axial fuel staging and hydrogen blending ratios enhances temperature uniformity and outlet temperature in the combustion chamber. The difference is that a higher fuel axial staged ratio leads to fuel accumulation around the central tube, reducing the temperature in the central fuel hole influence zone. 2) The increase in axial fuel staging ratios hindered complete fuel oxidation, but the addition of more than 30% H_2 improves incomplete combustion in local fuel-rich zones. However, hydrogen blended could not completely eliminate the negative impact of weakening mixing on the elevation of CO levels due to the limited diffusion capacity and delayed mixing location. 3) Variations in the axial fuel staged ratio resulted in inconsistent impacts of H_2 on NO_x levels: under higher and lower staged ratios (0.3 and 0.7), H_2 increased NO_x emissions; and under the condition of a staged ratio of 0.5, NO_x emissions were initially inhibited. At 30% H_2, the outlet NO_x concentration was 115.78 mg m^{-3}, which was 44% and 48% lower than that when the staged ratios were 0.3 and 0.7, respectively. Therefore, it was necessary to set the axial staged fuel ratio to 0.5 to ensure effective axial staging and NO_x inhibition capability during the CH_4–H_2 mixed combustion.

Acknowledgements

The authors acknowledge the financial support provided by Changzhou Key R&D Plan (Social Development Technology Support) of China (no. CE20225054), the Green Process Equipment Key Laboratory of Jiangsu Provincial University (no. GPE202401), and the Natural Science Foundation of Jiangsu Province (no. BK20230634).

Conflict of Interest

The authors declare no conflict of interest.

Author Contributions

Xiaochen Yu: methodology; writing—review and editing; data curation. **Yujie Zhao**: supervision; writing—original draft; formal analysis. **Zhen Zhang**: resources; validation. **Feichi Zhang**: software; writing—review and editing. **Lin Liu**: funding acquisition; project administration.

Data Availability Statement

Research data are not shared.

Keywords

axial staged combustion, computational fluid dynamics, CH_4–H_2 mixture combustion, NO_x, swirls

[1] IEA, World Energy Outlook **2022**, https://www.iea.org/reports/world-energy-outlook-2022.
[2] M. Sekar, T. A. Alahmadi, S. Nithya, *Fuel* **2024**, *370*, 131807.
[3] Y. Wang, X. Zhang, Y. Li, *Int. J. Hydrogen Energy* **2023**, *48*, 7122.
[4] O. Kumuk, *Fuel* **2025**, *381*, 133590.
[5] G. E. Marin, A. V.A. R. TitovAkhmetshin, A. R. Akhmetshin, A. V. Ishalin, *Int. J. Hydrogen Energy* **2025**, *97*, 649.
[6] D. Wang, Z. Tan, J. Xu, H. Meng, *Int. J. Hydrogen Energy* **2024**, *53*, 409.
[7] MEE of China, Emission standards for air pollutants from boilers, GB 13271 **2014**, https://www.mee.gov.cn/ywgz/fgbz/bz/bzwb/dqhjbh/dqgdwrywrwpfbz/201405/t20140530_276318.shtml.
[8] P. Rajpara, R. Shah, J. Banerjee, *Appl. Therm. Eng.* **2025**, *267*, 125844.

[9] B. Liu, B. Bao, Y. Wang, H. Xu, *J. Energy Inst.* **2017**, *90*, 441.
[10] S. Xu, C. Dou, S. Tian, L. Xi, H. Liu, *Fuel* **2025**, *380*, 133179.
[11] H. Liu, Z. Zeng, K. Guo, *Appl. Therm. Eng.* **2023**, *219*, 119460.
[12] A. M. Elbaz, H. A. Moneib, K. M. Shebil, W. L. Roberts, *Renew. Energy* **2019**, *138*, 303.
[13] W. Wang, Y. Li, X. Cheng, F. Lin, *J. Eng. Therm. Energy Power* **2020**, *35*, 34.
[14] G. Lopez-Ruiz, I. Alava, J. M. Blanco, *Energy* **2023**, *270*, 126882.
[15] W. Qin, J. Shi, Q. Cheng, *Fuel* **2025**, *381*, 133605.
[16] S. Ren, W. P. Jones, X. Wang, *Fuel* **2023**, *334*, 126582.
[17] M. S. Cellek, A. Pınarbaşı, G. Coskun, U. Demir, *Fuel* **2023**, *343*, 127905.
[18] M. Liu, C. Jiang, B. C. Khoo, H. Zhu, G. Gao, *J. Comput. Phys.* **2024**, *501*, 112783.
[19] G. D. Raithby, E. H. Chui, *J. Heat Transfer.* **1990**, *112*, 415.
[20] H. Fan, J. Feng, W. Bai, H. Wang, N. Akkurt, W. Li, J. Gao, O. AliAkbaria, Q. Xu, *Fuel* **2023**, *346*, 128321.
[21] B. Wang, W. Wei, S. Ma, G. Wei, *Int. J. Hydrogen Energy* **2016**, *41*, 19191.
[22] M. Choi, Y. Park, X. Li, Y. Sung, S. Park, K. Moon, G. Choi, *Fuel* **2019**, *253*, 887.
[23] X. Su, L. Ma, Q. Fang, C. Yin, H. Zhuang, Y. Qiao, C. Zhang, G. Chen, *Appl. Therm. Eng.* **2024**, *238*, 122043.
[24] Z. Hu, E. Jiang, X. Ma, *J. Cleaner Prod.* **2019**, *233*, 650.
[25] S. Tamang, J. Son, H. Park, *Fuel* **2025**, *387*, 134377.
[26] Y. B. Zeldvich, *Acta Phys. Chim. Sin.* **1946**, *21*, 577.
[27] H. Pan, S. Geng, H. Yang, G. Zhang, H. Bian, Y. Liu, *Int. J. Hydrogen Energy* **2023**, *48*, 784.
[28] J. W. Bozzelli, A. M. Dean, *Int. J. Chem. Kinet* **1995**, *27*, 1097.
[29] A. N. Hayhurst, E. M. Hutchinson, *Combust. Flame* **1998**, *114*, 274.
[30] T. F. Smith, Z. F. Shen, J. N. Friedman, *J. Heat Transfer* **1982**, *104*, 602.
[31] A. M. García, M. A. Rendon, A. A. Amell, *Fuel* **2020**, *276*, 118013.
[32] B. Li, X. Yang, N. Yu, S. Bu, S. Zhang, W. Dai, X. Wang, S. Suo, J. Liu, L. Jiang, *Appl. Therm. Eng.* **2025**, *264*, 125405.
[33] Z. Wang, X. Liu, J. Liu, Y. Xu, W. Gu, J. Zheng, *Int. J. Hydrogen Energy* **2025**, *102*, 80.
[34] M. K. Büyükakın, S. Öztuna, *Int. J. Hydrogen Energy* **2020**, *45*, 35246.
[35] P. J. Roache, *Annu. Rev. Fluid Mech.* **1997**, *29*, 123.
[36] L. Yang, S. Fang, *J. Beibu Gulf Univ.* **2023**, *38*, 63.
[37] G. P. Smith, D. M. Golden, M. Frenklach, N. W. Moriarty, B. Eiteneer, M. Goldenberg, C. T. Bowman, R. K. Hanson, S. Song, W. C. Gradiner, V. V. Lissianski, GRI 3.0 Mechanism; Available from: http://www.me.berkeley.edu/gri_mech/.
[38] W. Gao, Y. Yan, L. Huang, W. Zhang, K. Shen, *Int. J. Hydrogen Energy* **2021**, *46*, 40105.
[39] W. Du, S. Zhou, H. Qiu, J. Zhang, Y. Fan, *Case Stud. Therm. Eng.* **2022**, *39*, 102468.
[40] Y. Liu, Z. Liang, F. Bao, *Chin. Sci. Technol. Info.* **2010**, *12*, 37.
[41] M. K. Ghareh Gheshlaghi, A. M. Tahsini, *Int. J. Hydrogen Energy* **2023**, *48*, 33732.
[42] J. Xiao, Q. Liu, S. He, S. Wang, Z. Zhang, *Int. J. Hydrogen Energy* **2024**, *65*, 50.
[43] K. Cheng, P. Wang, C. Mao, A. Valera-Medina, Y. Wang, Z. Yang, W. Liu, F. Tian, *J. Combust. Sci. Technol.* **2023**, *29*, 561.
[44] D. Wei, S. Han, X. Ji, T. Wang, B. Sun, *J. Energy Inst.* **2024**, *113*, 101558.
[45] S. Devanesan, M. S. Alsalhi, N. Asemi, G. Arunkumar, *Fuel* **2023**, *353*, 129137.
[46] Z. Lai, W. Song, Q. Wang, S. Wang, *Energy* **2025**, *320*, 135048.
[47] L. Cheng, W. Li, S. Peng, C. Chai, W. Wang, C. Tian, J. Zhang, L. Liu, H. Zhang, Y. Zhang, *Int. J. Hydrogen Energy* **2024**, *92*, 590.
[48] P. Rajpara, R. Shah, J. Banerjee, *Int. J. Hydrogen Energy* **2018**, *43*, 17505.
[49] D. Han, K. Song, J. Huo, X. Li, C. Xu, *Appl. Therm. Eng.* **2025**, *260*, 124995.
[50] C. Lu, Y. Lyu, C. Xing, P. Qiu, L. Zhang, *Int. J. Hydrogen Energy* **2025**, *130*, 9.
[51] A. D. Prithu, K. M. Rahman, M. R. Islam, D. H. Saharaj, M. S. Hossain, *Int. J. Thermofluids* **2025**, *26*, 101112.
[52] X. Jiang, P. Li, J. Guo, F. Hu, F. Wang, J. Mi, Z. Liu, *Int. J. Hydrogen Energy* **2018**, *43*, 8534.